ACCSCIENCE PUBLISHING

Engineering Science in Additive Manufacturing

ORIGINAL RESEARCH ARTICLE

Vision-derived stability indicators from melt pool and wire dynamics in laser hot-wire directed energy deposition

Mario Rodriguez-Parra[1,2*], Miguel Hoffmann[2], Mithulan Paramanathan[2], Thomas Feldhausen[1,2], and Eric MacDonald[2,3]

[1]Aerospace and Mechanical Engineering, The University of Texas at El Paso, El Paso, Texas, United States of America

[2]Manufacturing Science Division, Oak Ridge National Laboratory, Tennessee, United States of America

[3]Industrial and Systems Engineering, University of Florida, Gainesville, Florida, United States of America

Abstract

Laser hot-wire directed energy deposition (LHW-DED) improves process performance by enhancing wire preheating. Reliable *in situ* assessment of process stability remains challenging because the melt-pool behavior and wire transfer are commonly evaluated separately. This study develops vision-derived stability indicators by jointly characterizing melt-pool geometry and wire dynamics during the deposition of stainless steel 316LSi under varying laser power and hot-wire power. Optical videos were analyzed using multi-Otsu segmentation for melt-pool area extraction and the Segment Anything Model 2 for temporal wire segmentation. Melt-pool area was used to characterize the energy input, while frame-to-frame Intersection over Union (IoU), IoU volatility, and angle variability were evaluated as indicators of wire stability. Low energy conditions produced smaller melt pools and greater wire flutter, whereas sufficient energy inputs produced larger melt pools and more consistent wire behavior. Parameter-level correlations showed that melt-pool area for single beads was related to penetration depth and total cross-sectional area measured by optical microscopy. Melt-pool area was also associated with wire stability during the single-bead laser-power sweep. These results establish melt-pool geometry and wire dynamics as complementary indicators of LHW-DED stability and support future process qualification and *in situ* feedback control.

Keywords: Laser hot-wire directed energy deposition; Computer vision; Additive manufacturing; In situ monitoring

***Corresponding author:**
Mario Rodriguez-Parra
(rodriguezpma@ornl.gov)

Citation: Rodriguez-Parra M, Hoffmann M, Paramanathan M, Feldhausen T, MacDonald E. Vision-derived stability indicators from melt pool and wire dynamics in laser hot-wire directed energy deposition. *Eng Sci Add Manuf.* 2026;2(4):026360019. doi: 10.36922/ESAM026360019

Received: September 1, 2026

Revised: October 2, 2026

Accepted: October 15, 2026

Published online: November 2, 2026

Copyright: © 2026 Author(s). This is an Open-Access article distributed under the terms of the Creative Commons Attribution License, permitting distribution, and reproduction in any medium, provided the original work is properly cited.

Publisher's Note: AccScience Publishing remains neutral with regard to jurisdictional claims in published maps and institutional affiliations.

1. Introduction

Directed energy deposition (DED) is a widely adopted metal deposition AM technology due to its ability to manufacture components with low production costs, high deposition rates, and suitability to build or repair large components.[1] DED processes utilize a focused thermal energy source such as an electron beam, electric arc, plasma arc, or laser to melt

feedstock to generate a localized melt pool on a previously deposited layer.[2–6] Laser hot-wire DED (LHW-DED) incorporates resistive preheating of the wire feedstock prior to interaction with the melt pool. This preheating increases the thermal state of the incoming wire, promoting a more stable and energy-efficient deposition process while also reducing the thermal gradient between the wire and the melt pool. The preheating enhances wetting, improves fusion quality, and increases penetration depth without significantly increasing bead width or height.[7,8] As a result, LHW-DED has been identified as a promising alternative to wire arc additive manufacturing for large-scale metal deposition, while retaining advantages associated with laser-based processes, including localized energy input, improved process control, and the ability to tune heat input through both independent laser and resistive preheating sources.[8]

Despite these advantages, LHW-DED is a complex process characterized by a narrow stability window.[8,9] Deviations in process parameters, specifically those related to the balance between energy and mass inputs such as laser power, wire feed speed, and resistive preheating, can lead to distinct defect morphologies and unstable deposition behavior.[10] While all DED processes are susceptible to instabilities related to heat input, melt-pool geometry, and defect formation, wire-fed DED introduces an additional stability challenge through direct mechanical interaction between the wire and the melt pool. In these systems, instabilities are commonly identified through macroscopic phenomena such as stubbing and dripping and are characterized by fluctuations in wire position and orientation.[9,11] In this work, such fluctuations are referred to as wire flutter, defined as rapid lateral movements of the wire relative to the melt pool, as opposed to steady wire position, which is necessary to provide consistent geometry and improved resolution.

Stubbing occurs when insufficient energy prevents complete wire melting before impacting the underlying structure, causing mechanical vibrations and potential damage to the deposition head.[12,13] Conversely, dripping arises from excessive heat input, where the wire melts prematurely above the substrate, disrupting the continuous liquid transfer and causing globular droplet formation.[14,15] Both instabilities can lead to variations in bead geometry, high residual stresses, and microstructural heterogeneity.[16–18] Maintaining a stable wire-to-melt-pool relationship is necessary to achieve consistent geometry and structural integrity.[19]

In related wire-based processes such as wire arc additive manufacturing, process stability is often assessed through continuous observation by an operator, requiring rapid intervention to identify and rectify anomalies within seconds. Consequently, automated monitoring strategies based on computer vision algorithms and real-time signal extraction have emerged as solutions for integration into closed-loop process control systems.[20] While melt-pool behavior has been investigated using thermography and optical imaging techniques,[9,12,21–25] wire-fed processes pose a specific challenge regarding the wire position and motion, which are critical factors affecting process stability.

Early monitoring approaches for DED relied primarily on conventional computer vision methods, where image segmentation separates process-relevant regions or features from the surrounding image background, commonly using techniques such as intensity thresholding and edge-based boundary detection.[26,27] However, their performance is highly dependent on imaging conditions, signal contrast, and process conditions. When the melt pool exhibits strong intensity separation from the background and limited interference from other process features, such as the wire, spatter, and reflections, these methods can provide reliable frame-adaptive segmentation with minimal computational overhead. In more complex or highly variable DED conditions, however, their robustness can degrade, motivating the use of learning-based approaches.[20,28] To overcome these limitations, deep learning architectures such as convolutional neural networks—especially the U-Net architecture,[29–31] the region-based convolutional neural network,[32,33] and self-supervised frameworks[25,34]—have demonstrated superior capability in isolating melt-pool features under more variable imaging conditions. Foundation models like the Segment Anything Model (SAM)[35] and its successors—SAM2[36] and SAM3[37]—have further expanded image and video segmentation capabilities with minimal retraining.[20]

However, most computer vision studies have focused primarily on melt-pool segmentation, geometric feature characterization, or identifying wire deposition states through wire tracking, image intensity variation, or temporal differences. In wire-DED, the wire introduces an additional dynamic interaction with the melt pool, yet quantitative wire motion indicators are less commonly evaluated together with melt-pool dimensions across controlled variations in process energy input. The relationship between melt-pool development and continuous wire dynamics remains insufficiently characterized as a combined indicator of process stability.

This study investigates the coupled evolution of melt-pool geometry and wire motion in LHW-DED under independent variations in laser power and hot-wire power. Multi-Otsu segmentation was used to extract the projected melt-pool area, while SAM2-based temporal segmentation

was used to quantify frame-to-frame wire intersection over union (IoU), IoU volatility, and wire angle variability. The evolution of these monitoring metrics was interpreted jointly to identify transitions between unstable and stable transfer behavior and to determine how these transitions depend on the energy input. The *in situ* measurements were further compared with post-process cross-sectional geometry from the melt pool, including width, height, and cross-sectional areas. The principal contribution is therefore the integration of melt pool and wire dynamics measurements into complementary and physically interpretable indicators of LHW-DED process stability.

2. Materials and methods

This section describes the Mazak metal hybrid system, imaging, and algorithms used to monitor hot-wire laser deposition process health.

2.1. Experimental setup

Experiments were conducted using a hybrid system (VTC-800G/SR AM, Yamazaki Mazak Corporation, Japan) equipped with a deposition head (FiberWELD DHc, Laser Mechanisms Inc., USA), an 8 kW nLight laser operating at 1,070 nm with a 150 μm fiber and integrated 5-axis machining capability. The additive head uses a single laser beam split into a tri-beam configuration that converges at the melt pool and enables coaxial wire feeding. A separate 1 kW power supply integrated within the head was used to resistively heat the wire, referred to as "hot-wire power." A schematic of the processing head configuration is shown in Figure 1.

A one-factor-at-a-time experimental design was used, in which laser power was varied while hot-wire power was held constant at 650 W, and hot-wire power was varied while laser power was held constant at 4,000 W. The same eight-bead deposition layout shown in Figure 2 was repeated for each of the 12 process conditions listed in Table 1. Conditions 1–6 correspond to the laser-power sweep from 3,000 to 5,500 W at a constant hot-wire power of 650 W, whereas conditions 7–12 correspond to the hot-wire power sweep from 0 to 1,000 W at a constant laser power of 4,000 W (Table 1). This design enabled the individual trends associated with each process parameter to be evaluated under a fixed level of the other parameter. However, the design does not permit statistical estimation of interaction effects between laser power and hot-wire power. No independently repeated deposition runs were performed for a given process condition.

2.2. *In situ* monitoring and image processing procedure

In situ data acquisition was performed using an optical camera (XIRIS XVC-1000, Xiris Automation Inc., Canada) mounted inside the deposition head at an inclination of approximately 8° relative to the deposition axis (Figure 1). The camera uses a monochromatic complementary metal-oxide semiconductor sensor with a dynamic range exceeding 140 dB and captures 16-bit image sequences at a spatial resolution of 1,080 × 1,024 pixels and a frame rate of 30 frames per second. The camera focus was adjusted manually before deposition to maintain consistent image quality across all experiments.

A multistage image processing pipeline was developed in Python (3.10, Python Software Foundation, Netherlands) to extract two complementary classes of *in situ* information from the recorded frame sequences: Projected melt-pool geometry and wire dynamics. As shown in Figure 3, the melt pool was segmented using a threshold image-processing method, while the wire was segmented using a prompt-based segmentation foundation model to improve robustness under changing local contrast, reflections, and process illumination. The resulting masks were then used to compute the geometric and temporal stability metrics.

Table 1. Variable process parameters used for laser power and hot-wire experiments

Process condition	Laser power (W)	Hot-wire power (W)
1	3,000	650
2	3,500	650
3	4,000	650
4	4,500	650
5	5,000	650
6	5,500	650
7	4,000	1000
8	4,000	850
9	4,000	700
10	4,000	550
11	4,000	200
12	4,000	0

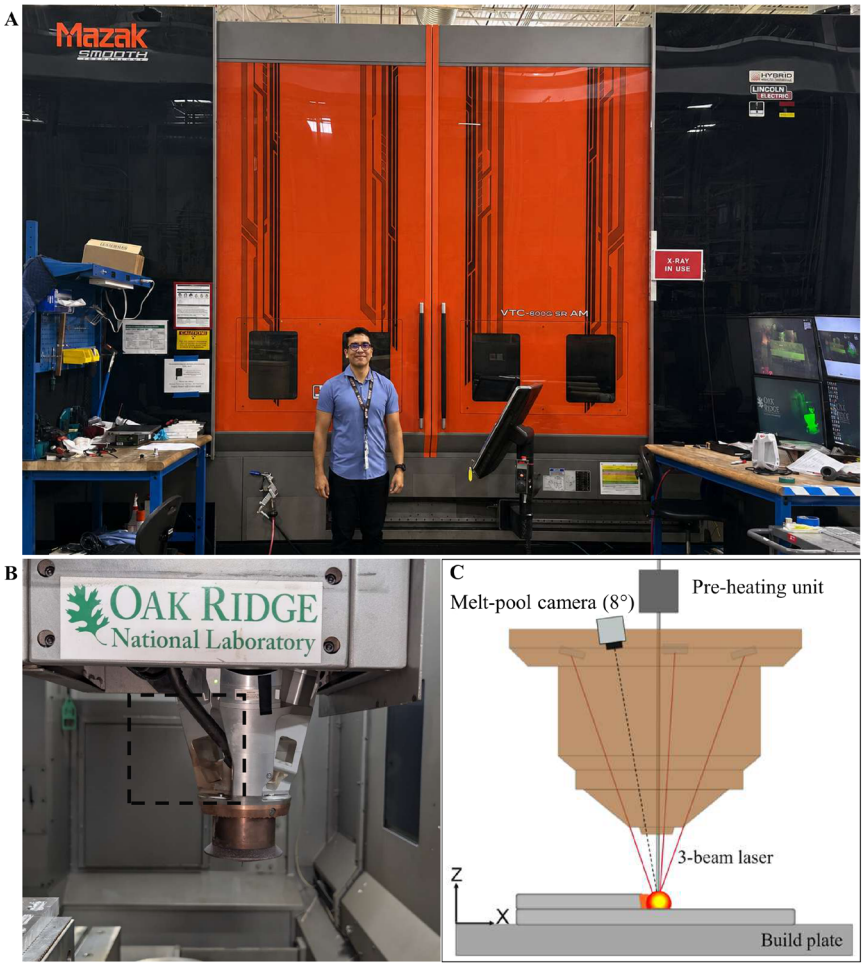


Figure 1. Laser hot-wire directed energy deposition system and melt-pool imaging configuration: (A) Mazak VTC-800 SR AM hybrid manufacturing system. (B) Close-up of the deposition head. (C) Schematic of the optical monitoring configuration, including the melt-pool camera positioned 8° from the process axis, the preheating unit, three-beam laser configuration, and build plate coordinate system.

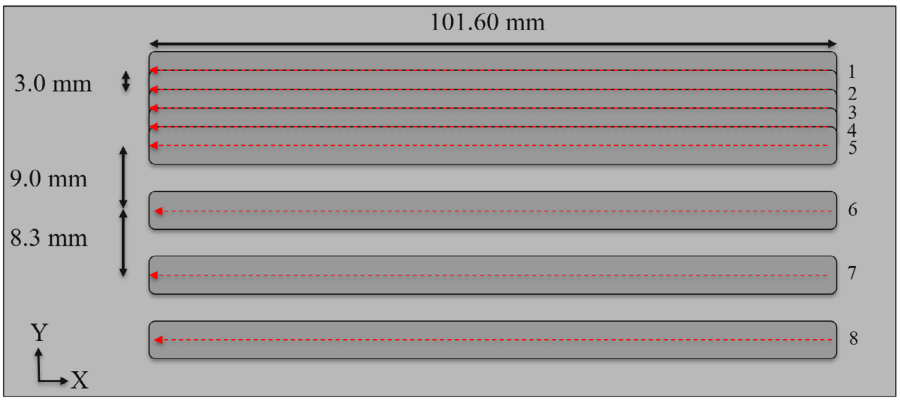


Figure 2. Two-dimensional deposition layout used for each of the 12 process conditions. Each condition consisted of eight deposited tracks: A five-bead pad (beads 1–5) and three spatially separated single beads (beads 6–8).

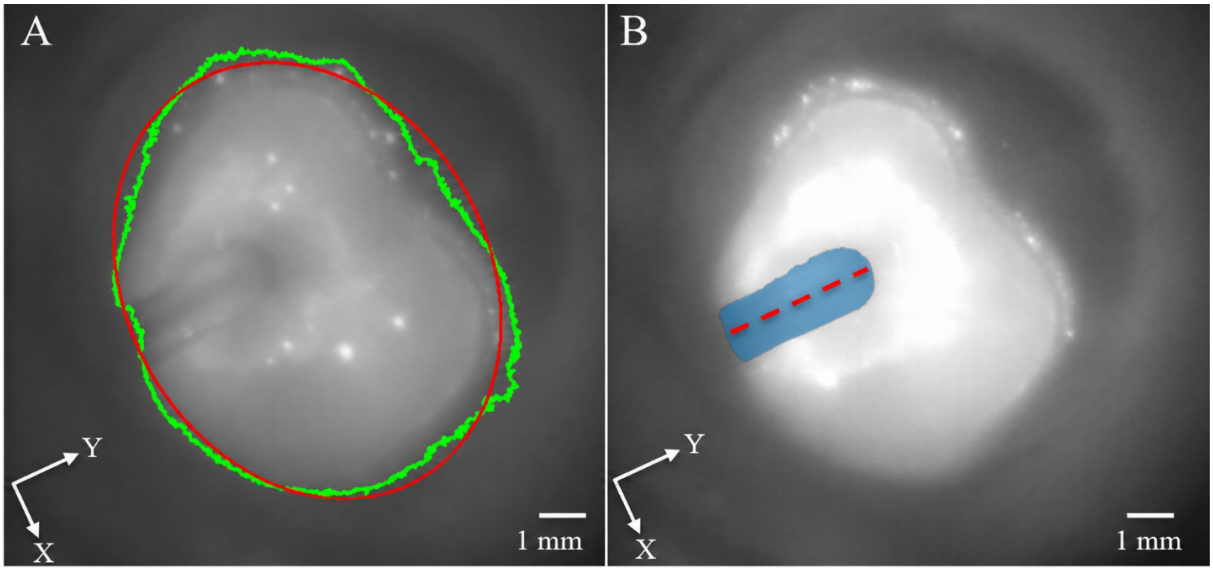


Figure 3. Representative examples of the segmentation procedures used for the required features. (A) A multi-Otsu segmentation of the projected melt-pool region on the X–Y plane, shown in green, with the fitted ellipse used for geometric analysis. (B) Segment Anything Model 2-generated mask, shown in blue, with the principal wire axis shown as a dashed red line for extraction of the projected wire-angle metric.

The reported mean and standard error of the mean values from the melt pool and wire metrics were calculated from the frame-level observations within each geometry and process condition. Variability was reported as either the standard error of the mean or the 95% confidence interval (CI), as indicated in the respective figures and captions.

2.2.1. Melt-pool geometry

The projected melt-pool geometry on the X–Y plane was extracted using a multi-Otsu[38] grayscale thresholding approach. The original Otsu method determines an intensity threshold by maximizing the between-class variance of the image histogram, and its multilevel extension allows separation of multiple intensity classes within the same frame. In this work, the method was used to isolate the high-intensity melt-pool region from the surrounding background and lower-intensity image features under varying process conditions.

Since image intensity changes with the energy input, the segmentation was performed on a frame-to-frame basis rather than using a single global threshold for the full dataset. The resulting binary masks were processed in OpenCV (4.11.0.86, OpenCV, USA) to isolate the dominant connected region associated with the melt-pool zone. The melt-pool area and projected spatial dimensions were then extracted from the segmented masks on the X–Y plane as shown in Figure 3A. This threshold-based method was selected because it provided computationally efficient and repeatable segmentation across the image sequence while preserving sensitivity to process-induced changes in the melt-pool shape. Since the wire appears within the same field of view as the melt pool, the thresholded melt-pool mask also included part of the projected wire region across all process conditions. To quantify this contribution, the intersection between the melt pool and the wire masks was calculated for a 120-frame subset, consisting of 10 randomly selected frames from each of the 12 experimental conditions. The overlap was expressed as a percentage of the total thresholded melt-pool mask area for each frame.

2.2.2. Computer vision-based wire tracking and segmentation

Wire segmentation was performed using SAM2, which provided improved temporal consistency and robustness against background noise, illumination variability, and local reflections compared to statistical threshold algorithms. The implemented pipeline used the pre-trained SAM2 "sam2.1_hiera_small.pt" checkpoint and combined interactive point prompting on a reference frame with temporal mask propagation across the remaining frames in the video sequence.

All available deposition frames were included in the wire analysis. Each bead contained approximately 500 frames acquired at 30 frames/s, corresponding to approximately 16.7 s of analyzed deposition time per bead.

Since each process condition consisted of a five-bead pad and three single beads, approximately 4,000 frames were analyzed for each process condition. A single reference frame was manually initialized for each process condition, requiring the wire body and wire tip to be clearly visible and distinguishable from the surrounding melt-pool region. Positive point prompts were placed along the visible wire body and near the wire tip, while negative prompts were positioned on the adjacent melt pool and background regions. The initialized wire mask was subsequently propagated through the remaining frames using the SAM2 video-prediction framework. The schematic workflow of the SAM2 model is shown in Figure 4.

The resulting wire masks were used to quantify the frame-to-frame wire motion and stability metrics described in the next section. A physical calibration was performed by imaging a 1 mm gauge block under the same optical configuration used during deposition, resulting in a calibration factor of 74.5 pixels per mm. This conversion factor was applied to transform the feature dimensions into physical units where needed.

2.3. Wire motion and stability metrics

To characterize the wire dynamics, three metrics were extracted from the SAM2-generated wire masks on the projected X–Y plane: IoU, IoU volatility, and angle variability. IoU has previously been used as an indicator for wire motion and process stability in DED monitoring because it quantifies the spatial consistency of a segmented feature between consecutive frames.[39,40] In the present work, the IoU was calculated by comparing the mask of the current frame (M_t) to the mask of the immediately preceding frame (M_{t-1}) (**Equation 1**):

$$IoU\left(\%\right)=\frac{\left|M_t \cap M_{t-1}\right|}{\left|M_t \cup M_{t-1}\right|}\times 100 \tag{1}$$

Higher IoU values indicate a greater frame-to-frame consistency in wire position and shape, whereas low IoU values indicate large positional or morphological changes associated with unstable transfer behavior. In this study, sustained IoU values above approximately 80% were interpreted as characteristic of stable wire feeding conditions.

To quantify the temporal instability of the wire during deposition, the IoU volatility was calculated as the absolute change in IoU between consecutive temporal steps (**Equation 2**):

$$V_{IoU}=\left|IoU_t-IoU_{t-1}\right| \tag{2}$$

This metric is inversely related to process stability. High V_{IoU} values indicate rapid changes in the spatial overlap of the wire mask and therefore correspond to stronger wire flutter or intermittent transfer behavior.

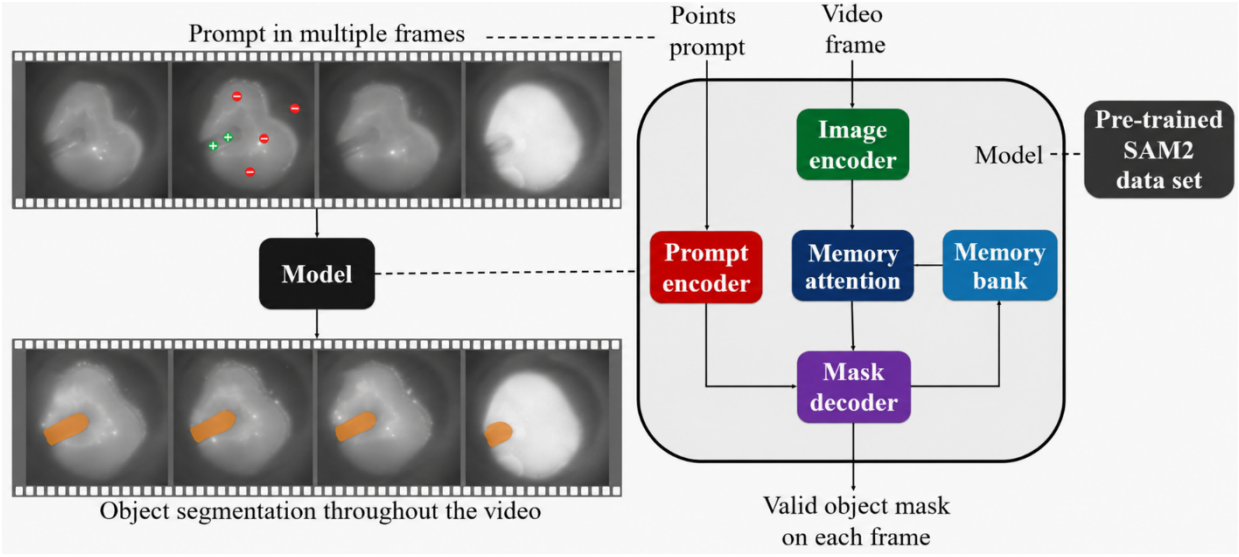


Figure 4. Schematic of the Segment Anything Model 2-based wire-segmentation workflow used in this study. A reference frame was initialized with positive and negative point prompts, after which the model propagated the wire mask throughout the video sequence using memory-assisted temporal tracking.[36]

A third metric, wire angle variability ($\Delta\theta$), was calculated from each frame using the orientation of the wire mask principal axis (X–Y). Let θ_t represent the projected principal axis angle of the wire at frame *t*. The frame-to-frame angular variation was calculated as (**Equation 3**):

$$\Delta\theta = \left|\theta_t - \theta_{t-1}\right| \quad (3)$$

This metric captures changes in the projected wire orientation and was used as an additional indicator of wire dynamic stability. As the angle is derived from a projected view, the measured value is most sensitive to motion visible on the imaging plane and does not resolve all three-dimensional components of wire motion equally. For each video, IoU, V_{IoU}, and $\Delta\theta$ were first calculated on a frame-by-frame basis. The resulting values were then grouped by deposition geometry, namely the single beads and the multi-bead pad. Geometry-specific means and 95% CIs were calculated for each process condition for all the process variable conditions.

An additional validation of the SAM2 segmentation was performed using manually annotated reference masks spanning all investigated process conditions and the same 120-frame subset used for the melt pool/wire overlap analysis. Manual annotations were generated from the original images using the same target definition applied in the automated segmentation. The SAM2-generated masks were compared with the corresponding manually annotated masks using IoU. In addition, the projected wire orientation was calculated from both masks using the same principal component analysis-based approach, and the absolute angular difference between the SAM2 and manual masks was used to quantify the effect of segmentation error on the extracted wire-angle metric.

2.4. Post-process analysis

Post-process optical microscopy was performed on cross-sections in the Y–Z plane to relate the *in situ* imaging results to the resulting fusion geometry. A total of two cross-sections per process condition were prepared from the single bead samples. The quantitative cross-sectional analysis was focused on the single beads because their isolated geometry provided a clearer basis for evaluating the direct effects of laser and hot-wire power on bead profile, penetration, and dilution. In contrast, the multi-bead pad includes bead overlap, local remelting, and cumulative thermal effects that complicate direct comparison of individual cross-sectional features between process conditions. Therefore, equivalent ex-situ Y–Z validation was not performed for the pad geometry, and pad-specific stability trends were evaluated using the *in situ* X–Y melt pool and wire-dynamics indicators The cross-sections were mounted in epoxy, ground using 500-, 800-, 1,000-, and 2,000-grit silicon carbide discs, polished using 6, 3, and 1 µm diamond suspensions with DP-Lubricant Purple, and finally vibratory polished using a 0.05 µm suspension with colloidal silica. The prepared specimens were optically imaged using a microscope (DM4000M, Leica, Germany) at a resolution of 0.97 µm/pixel at 5× magnification using bright-field imaging.

The obtained microscopy images were segmented using the base SAM2 small checkpoint to isolate the bead and dilution regions using the same prompt segmentation method described in Section 2.2.2. From these segmented masks, bead width, bead height, dilution depth, bead area, dilution area, total cross-sectional area, and dilution ratio were extracted as shown in Figure 5. This post-process analysis provided a physical Y–Z complement to the *in situ* X–Y measurements, allowing the projected melt-pool

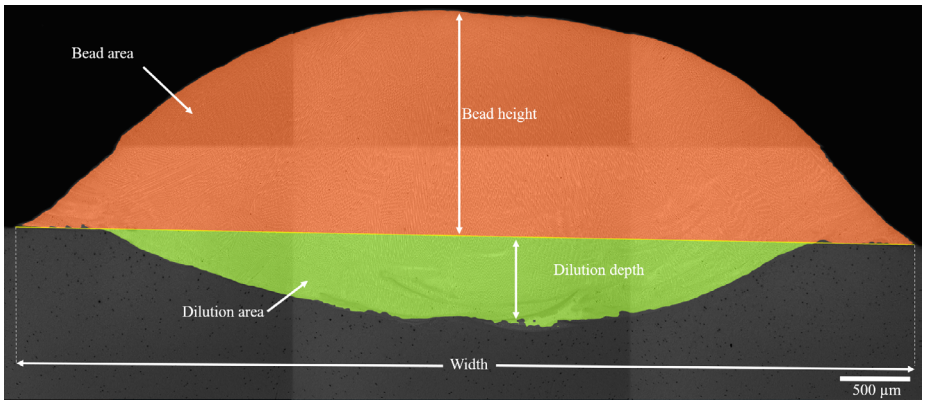


Figure 5. Representative cross-section of a single bead showing the geometric features extracted during post-process dimensional analysis, including bead area, bead height, width, dilution area, and dilution depth.

areas and wire stability metrics to be interpreted alongside the corresponding melt-pool morphology. The mean and corresponding 95% CIs were calculated from the two cross-sectional measurements obtained for each process condition.

2.5. Statistical correlation analysis

The cross-sectional data were correlated with the *in situ* optical process signatures to evaluate associations between the monitoring metrics and the resulting deposition behavior. The correlation analysis was performed across the six laser-power conditions using condition-level means from the single-bead specimens. The mean melt-pool area obtained from multi-Otsu segmentation was paired with the corresponding mean penetration depth and total cross-sectional area measured by optical microscopy. For the wire-stability correlation, the mean melt-pool area from the single beads was paired with the corresponding mean frame-to-frame wire IoU obtained from the SAM2 segmentation for each laser-power condition. Pearson's correlation coefficient (r) was used to quantify the strength and direction of each linear association. Because only six processing conditions were available, statistical significance was evaluated using a two-sided permutation test. All $6! = 720$ possible permutations of the response-variable labels were evaluated, and the exact probability was calculated as the proportion of permutations producing an absolute correlation coefficient equal to or greater than the observed value. Ordinary least-squares linear regression was used for visualization, and the coefficient of determination (R^2) was reported to describe the proportion of between-condition variance associated with the fitted linear relationship. To assess the sensitivity of the correlations to individual processing conditions, a leave-one-condition-out (LOO) analysis was additionally performed by removing each laser-power condition and recalculating r and R^2.

3. Results and discussion

The following section examines melt pool and wire behavior to define process stability indicators for feedback control.

3.1. Melt-pool area from *in situ* imaging

The proposed image-processing pipeline enabled frame-by-frame extraction of the projected melt-pool area in the X–Y plane using multi-Otsu segmentation. The resulting binary masks were used to calculate the melt-pool area throughout deposition. For each process condition, the data were summarized in two ways: (i) A per-bead mean area ± 95% CI, used to evaluate bead-to-bead area evolution during the programmed deposition sequence (Figure 6), and (ii) an overall mean area per geometry ± 95% CI for each process condition to compare parameter sensitivity between laser power and hot-wire power (Figure 7).

3.1.1. Effect of laser power at constant hot-wire power

Figure 6A shows that the projected melt-pool area increased with laser power for both the pad and single-bead geometries. For the pad, the melt-pool area generally increased from early beads to later beads at all laser powers, indicating that the local thermal state and evolving topography influenced the projected footprint during the multi-bead sequence. This effect was more pronounced at lower laser powers, where the first bead exhibited the smallest footprint, and later beads approached a more stable value by beads 3–5. At higher laser powers, bead-to-bead variation was smaller but still observable, suggesting that local thermal history continued to influence spreading even when laser power dominated melt-pool size.

In contrast, single beads showed less variation among tracks, consistent with their isolated geometry and reduced interaction with neighboring deposits. The difference between the two geometries indicates that the projected melt-pool area is affected not only by the imposed process parameters, but also by the local deposition environment. During pad deposition, each successive bead is deposited adjacent to material that has already been heated and solidified; consequently, local substrate conditions evolve through thermal accumulation, partial remelting of neighboring material, and changes in surface topography. These effects explain why the pad exhibited stronger bead-to-bead evolution than the isolated single beads, particularly at lower laser powers. The values in Figure 6A confirm that laser power primarily drove projected melt-pool area growth. The area of the pad beads increased from approximately 19 mm^2 at 3,000 W to 24 mm^2 at 5,500 W. A similar trend was observed for the single beads, which increased from approximately 18 mm^2 at 3,000 W to 23–24 mm^2 at 5,500 W. This behavior is expected because higher laser power increases the energy delivered directly into the melt-pool region, thereby enlarging the molten footprint visible in the image plane. In the context of process monitoring, this result indicates that projected melt-pool area is a sensitive descriptor of laser power-driven changes in the process state, particularly for identifying whether the system is operating in a lower or higher energy regime. However, the bead behavior shows that the projected area is not controlled by laser power alone. The larger bead-to-bead variation within the pad, especially at lower laser powers, suggests that thermal history and local deposition geometry affect the apparent footprint and should be considered when interpreting projected data. Therefore, while melt-pool area is highly useful as a monitoring

metric, it should be interpreted as a process state indicator rather than as a purely direct measure of energy input.

3.1.2. Effect of hot-wire power at constant laser power

Results shown in Figure 6B indicate that varying hot-wire power produced a comparatively weaker and non-monotonic effect on the melt-pool area than varying the laser power. The melt-pool area from the pads remained within a relatively narrow band across the hot-wire power range, with only modest evolution. For the single beads, however, the most pronounced deviation occurred at 0 W, which yielded a larger melt-pool footprint than the preheated conditions. This behavior is reflected in the mean values per power in Figure 7. The mean melt-pool area from the pad showed no strong dependence on hot-wire power. For the single beads, the 0 W hot-wire condition produced the largest mean melt-pool area (~23 mm^2), followed by a reduction at 200 W and a gradual return toward the values measured at higher hot-wire powers.

To evaluate whether the enlarged projected melt-pool area at 0 W could be attributed to inclusion of the projected wire within the thresholded mask, the wire–melt-pool overlap was quantified across all 12 process conditions. The projected wire accounted for approximately 7% of the segmented melt-pool area, with condition-level mean overlap values ranging from 6.17% to 7.94%. The 0 W hot-wire condition showed an overlap of 6.82%, comparable to the remaining conditions. Therefore, the larger projected footprint observed at 0 W was not associated with an unusually high contribution from the wire projection.

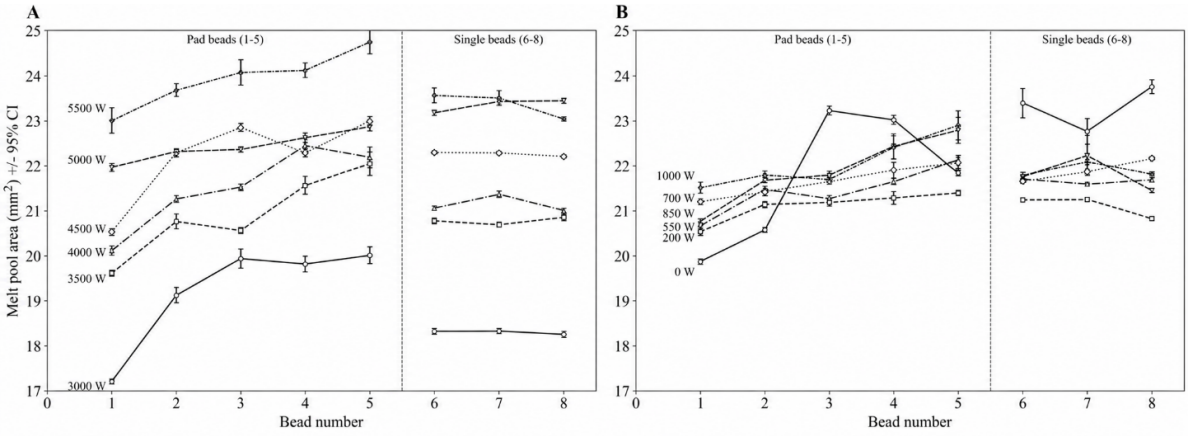


Figure 6. Per-bead mean melt-pool area (±95% confidence interval [CI]) extracted from coaxial imaging on the X–Y plane using multi-Otsu segmentation under (A) laser power variation and (B) hot-wire power variation. Beads 1–5 correspond to the pad; beads 6–8 correspond to the three single beads.

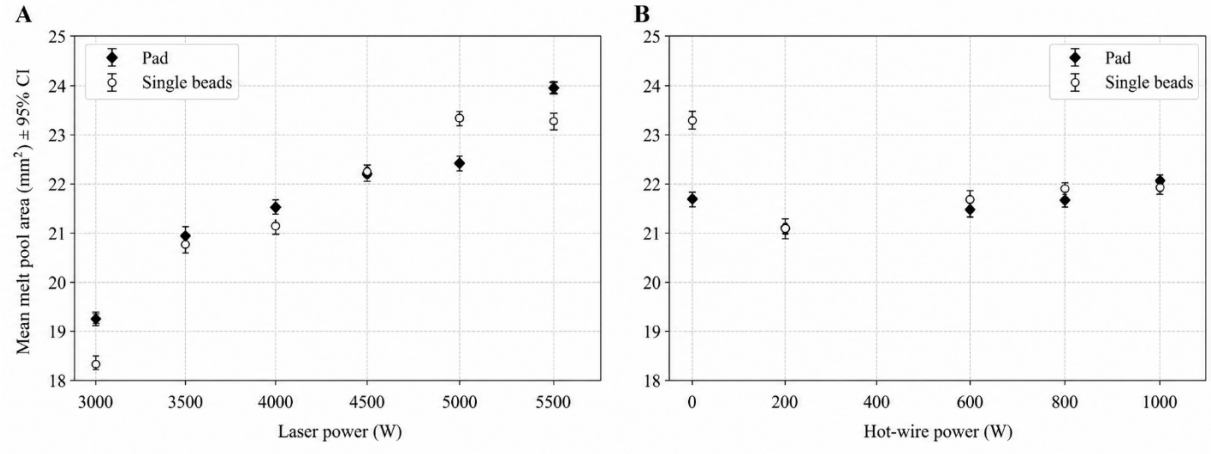


Figure 7. Overall mean melt-pool area (± 95 % confidence interval [CI]) extracted from *in situ* optical imaging on the X–Y plane using multi-Otsu segmentation for pad beads and single beads under (A) laser-power variation at a constant hot-wire power of 650 W and (B) hot-wire-power variation at a constant laser power of 4,000 W.

As the enlarged area footprint at 0 W does not follow the monotonic trend expected for a purely thermal input effect, it should not be interpreted simply as evidence of improved melting. Instead, the result is more consistent with unstable cold wire transfer. When resistive preheating is absent, the wire enters the melt pool at lower enthalpy, increasing the probability of intermittent wire–melt-pool contact, local perturbation of the molten region, and wire flutter.[9] These instabilities can mechanically perturb the molten region and promote lateral spreading, thereby enlarging the apparent footprint measured on the X–Y plane even without a corresponding increase in useful thermal coupling.

Once resistive preheating is introduced, the wire approaches the melt pool in a more favorable thermal state, reducing transfer instability and making the projected footprint more repeatable. This interpretation is important because it shows that projected melt-pool area alone can become ambiguous near the stability boundary. In other words, a larger footprint is not always equivalent to a better or more stable condition. For this reason, the melt-pool area results should be interpreted together with the wire stability metrics discussed later in this section.

These results demonstrate that melt-pool area extracted from coaxial imaging is strongly sensitive to laser power, while the response to hot-wire power is comparatively limited once stable transfer is achieved. This is consistent with the role of hot-wire power as an indirect energy input mechanism that primarily conditions the wire and improves transfer stability rather than substantially increasing melt-pool footprint.[8] These findings motivate joint interpretation of melt-pool geometry and wire flutter metrics, particularly under cold-wire or near-instability regimes where mechanical coupling can produce non-intuitive footprint trends.[9,41]

3.2. Wire stability metrics from Segment Anything Model 2 segmentation

Wire stability was quantified using a SAM2-based segmentation pipeline and a frame-by-frame IoU analysis of the segmented wire masks. In this framework, IoU captured the spatial consistency of the wire between consecutive frames, while IoU volatility and angle variability provided complementary measures of dynamic instability. The analysis was performed separately for the single beads and the multi-bead pad, revealing a clear geometry dependence in the wire dynamics response. This geometry-specific analysis was necessary because the two deposition configurations represent different local process conditions, as observed in Section 3.1. This section is complementary to the melt-pool area analysis by showing why the projected footprint alone is insufficient for evaluating unstable operating conditions.

The current segmentation pipeline used the pre-trained SAM2 checkpoint without additional fine-tuning on LHW-DED wire images, and its segmentation accuracy was quantitatively evaluated against manually annotated reference masks. A total of 120 frames were manually annotated, with 10 frames randomly selected from each of the 12 experimental conditions. The mean segmentation IoU was 0.852 ± 0.055 (standard deviation), with a median of 0.865, indicating strong spatial consistency. Additionally, because the segmented masks were used to determine projected wire orientation, we evaluated the effect of segmentation differences. The mean absolute angular difference between SAM2 and the manually annotated masks was 2.71 ± 2.43° (standard deviation), with a median error of 2.22°. Previous evaluations of promptable segmentation models show that segmentation performance depends strongly on object morphology, image contrast, and prompt ambiguity, with reported IoU values varying considerably across applications.[42,43] In the present study, the IoU and angular error values show that the pre-trained SAM2 checkpoint segmented the wire consistently without specific fine-tuning.

3.2.1. Intersection over Union as a process stability indicator

Figure 8 presents two representative cases that illustrate the difference between stable and unstable wire behavior. In the stable condition, the segmented wire remains confined to a narrow and repeatable trajectory, producing consistently high IoU values throughout most of the analyzed window. In contrast, the unstable condition exhibits abrupt changes in the segmented wire position and shape, resulting in intermittent IoU drops and temporal fluctuations. When separated by geometry, however, the results reveal that the stability transition differed between the single bead and pad geometries.

The results in Figure 9 show that the wire stability increased with laser power, but the transition was not identical for the single beads and the pad. The IoU values for single beads increased from approximately 35% at 3,000 W and 43% at 3,500 W to 90% at 4,000 W, indicating a sharp transition into a stable wire transfer regime. Above 4,000 W, the single beads maintained constant high IoU values above 85%. The pad followed the same general trend, but the transition was more gradual, with IoU values increasing from approximately 34% at 3,000 W and 47% at 3,500 W to 74% at 4,000 W, before reaching higher stable values at 4,500, 5,000 and 5,500 W. This indicates that the single beads reached stable transfer at a lower laser power

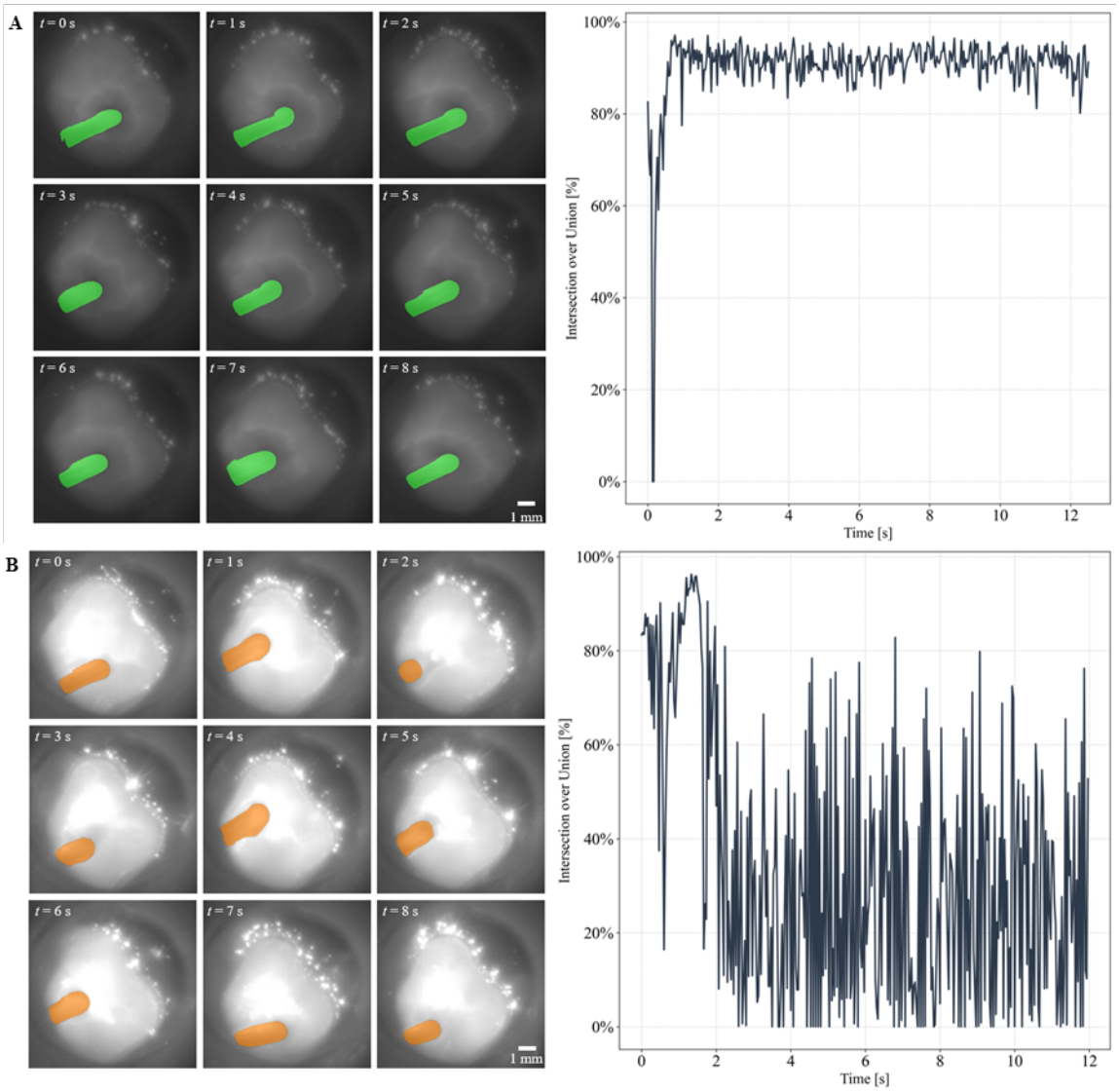


Figure 8. Intersection over Union trace over time. (A) High values indicate stable wire behavior at Laser power: 5,500 W, hot-wire power: 650 W. (B) Intermittent and low-value drops reveal process instability (Laser power: 4,000 W, hot-wire power: 0 W).

threshold, while the pad required higher laser power to reach a highly consistent wire behavior.

The hot-wire power variations showed an even stronger geometry-dependent behavior (Figure 9B). For the single beads, the IoU increased rapidly from approximately 26% at 0 W to 71% at 200 W, and exceeded 84% by 550 W, after which the values remained on a high-IoU plateau up to 1,000 W. This behavior indicates that the resistive preheating strongly improved wire stability in the isolated geometries. The pads, however, showed a lower and more gradual response across the same hot-wire power range, with IoU values increasing from 36% at 0 W to 67% at 1,000 W. Although this variable improved the pad response overall, it did not produce the same high IoU stability observed in the single beads at the same constant laser power.

This difference suggests that hot-wire power primarily conditions the incoming wire, whereas stable transfer in the pad also depends strongly on the local melt-pool environment. In the single beads, the wire interacts with a more isolated and geometrically simple molten region, allowing preheating to improve wire incorporation and reduce intermittent contact with the melt pool. During the pad deposition, however, successive beads interact with previously deposited material through partial remelting, residual heat accumulation, and geometric overlap.

The resulting changes in melt-pool shape, local surface inclination, and wire-to-surface interaction can alter the apparent wire position and its incorporation into the molten region. These effects are aligned with the lower IoU and higher IoU volatility and angle variability observed for the pad relative to the single beads under several process conditions. The geometry-dependent transition therefore indicates that the stability metrics respond not only to the energy input, but also to the local thermal and geometric state.

This interpretation is consistent with previous work showing that hot-wire preheating can improve transfer behavior and process stability in wire-fed laser deposition, while local geometric and thermal conditions still influence melt-pool behavior and deposition consistency.[8,9,15,39] As laser power increases, the melt pool becomes larger and more thermally developed, which can promote stronger thermocapillary circulation driven by surface-tension gradients and improve the ability of the melt pool to capture the wire more efficiently. This interpretation is consistent with the observed increase in IoU above the geometry-dependent threshold, although the present image analysis does not directly resolve melt-pool flow.

Similarly, the hot-wire experiment suggests that resistive preheating improves wire stability by increasing the thermal condition of the incoming wire before melt-pool contact. Preheating at ≥550 W was associated with higher IoU and more consistent wire transfer. In contrast, the pad did not reach the same high-IoU plateau, with a maximum mean IoU of approximately 67%. This indicates that although hot-wire preheating improves wire stability, stable transfer on the pad also depends on the local melt-pool environment. Together, these findings show that the stable operating window depends on the deposition geometry. Single beads transitioned to a high-IoU regime at approximately 4,000 W, whereas the pad exhibited a comparable transition at approximately 4,500 W. Because equivalent Y–Z cross-sectional validation was not performed for the pad geometry, the approximately 4,500 W value should be interpreted as an indicator-based stability transition specific to the investigated pad geometry rather than as an independently validated process threshold. Although the results suggest that wire-transfer stability is influenced by both wire preheating and the thermal state of the melt pool, the one-factor-at-a-time design used in this study does not allow the interaction between laser power and hot-wire power to be quantified. The hot-wire-power trends reported here therefore apply specifically to the investigated constant laser power of 4,000 W, while the laser-power trends correspond to a constant hot-wire power of 650 W.

3.2.2. Wire volatility and angle variability as stability metrics

The interpretation of the wire stability was further strengthened by the IoU volatility and angle variability metrics, which provided complementary information beyond the IoU values. Whereas IoU describes the average spatial consistency of the segmented wire between consecutive frames, IoU volatility quantifies how much that overlap changes over time. In this sense, volatility captures temporal instability: Low volatility indicates that the wire follows a repeatable trajectory from frame to frame, while high volatility indicates erratic or intermittent wire motion. Therefore, the combined use of IoU and volatility allows

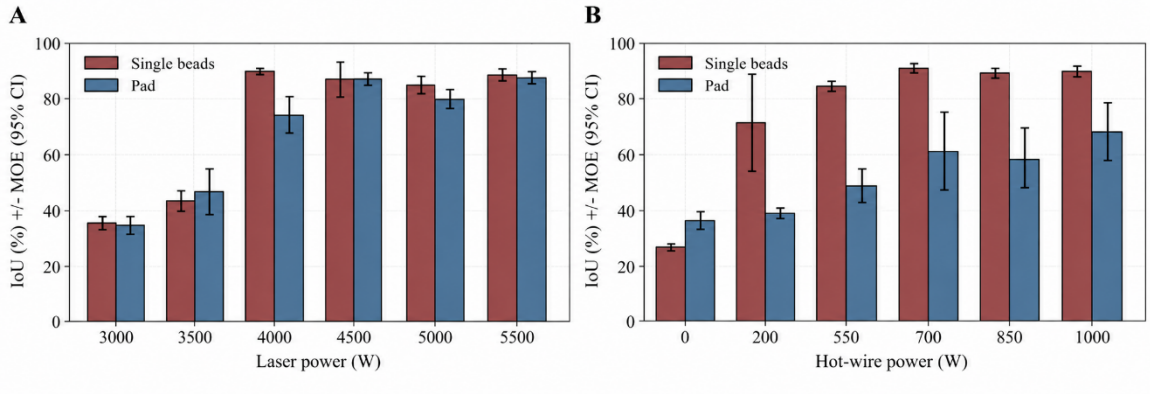


Figure 9. IoU values per geometry for the segmented wire as a function of (A) laser power and (B) hot-wire power. Error bars represent 95% CI. Higher IoU values indicate greater frame-to-frame wire shape and position consistency.
Abbreviations: CI: Confidence interval; IoU: Intersection over Union; MOE: Margin of error.

different process states to be distinguished more clearly, including stable behavior (high IoU, low volatility), fluttery but partially consistent behavior (high IoU, high volatility), persistently poor overlap (low IoU, low volatility), and unstable behavior with strong temporal fluctuations (low IoU, high volatility). A condition may exhibit moderate or even high mean IoU while still showing elevated volatility, indicating that the wire generally remains within the same region but undergoes intermittent abrupt displacements between consecutive frames.

Figure 10 shows that the volatility decreased with increasing laser power for both geometries, confirming the same stabilization trend identified by the IoU results. For the single beads, volatility was high at 3,000 and 3,500 W (approximately 0.27 and 0.25, respectively), then dropped to approximately 0.05 at 4,000 W. Above this threshold, the single beads remained in a low-volatility regime, indicating stable and repeatable wire motion. The pad followed the same general trend, but with consistently higher volatility over much of the laser power range. In particular, the pad still showed elevated volatility at 4,000 W and higher volatility at 5,000 W than at 4,500 and 5,500 W. This indicates that, although the IoU suggested generally stable transfer, the pad remained more susceptible to intermittent frame-to-frame fluctuations. Therefore, volatility adds useful information by revealing that temporal wire flutter may not be fully apparent from the IoU alone.

Stronger geometry dependence was observed in the hot-wire power sweep. Volatility from the single beads decreased from approximately 0.23 at 0 W to 0.14 at 200 W and 0.08 at 550 W, reaching a minimum near 550 W and remaining low through 1,000 W. This trend confirms that resistive preheating strongly improved the temporal stability of the wire in the isolated bead geometry. In contrast, the pad showed much higher volatility across the entire power range, decreasing from approximately 0.26 at 0 W to about 0.16 at 1,000 W. Thus, although increasing hot-wire power improved the pad response, it did not shift the system into the same low-volatility regime observed for the single beads. These results are consistent with the IoU trends and indicate that the pad remained more dynamically unstable at a constant 4,000 W of laser power, even as the hot-wire preheating increased.

The wire orientation results in Figure 11 provide an additional perspective on the same behavior. The wire orientation was further evaluated through a wire angle analysis that measures variability relative to the power input. In this off-axis monitoring configuration, the analysis is particularly sensitive to the wire lateral displacement in the X–Y plane and the resulting change in the inclination of the wire toward the melt pool. In the laser power experiment, the angle variability decreased from approximately 7° at 3,000–3,500 W to about 3° at 4,000 W and above. The pad again showed a more gradual response, decreasing from approximately 10° at low laser power to approximately 4° at higher powers. This confirms that the transition to stable wire transfer with increasing laser power was accompanied not only by improved mask overlap but also by a more consistent wire orientation.

The hot-wire power results showed the same tendency but with a stronger contrast between geometries. Angle variability for the single beads was highest at 0 W (approximately 11°) and dropped once preheating was introduced, reaching approximately 3° for most preheated

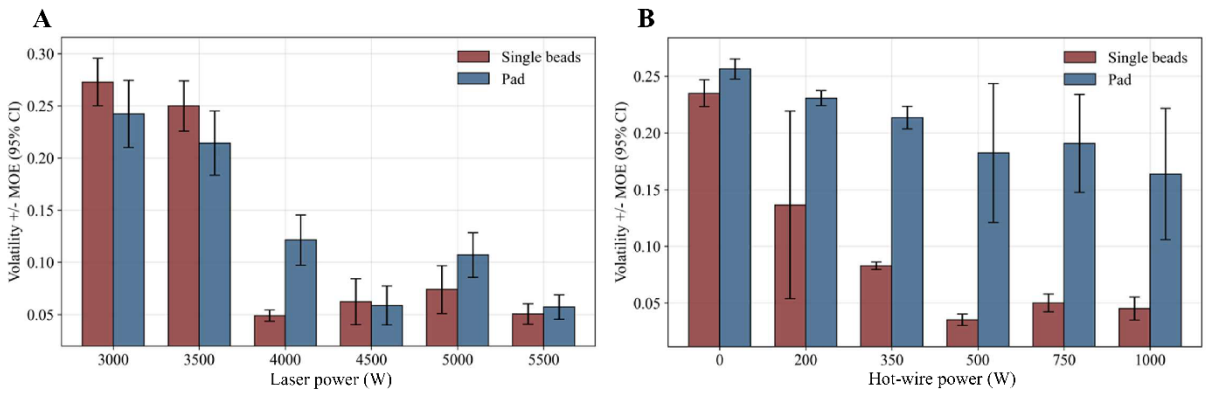


Figure 10. IoU volatility values per printed geometry for the segmented wire as a function of (A) laser power and (B) hot-wire power. Error bars represent 95% CIs. Higher volatility indicates larger frame-to-frame changes in wire overlap and therefore greater temporal instability.
Abbreviations: CI: Confidence interval; IoU: Intersection over Union; MOE: Margin of error.

conditions. In contrast, the pad maintained larger angular fluctuations across the hot-wire power range, decreasing more gradually from approximately 8° at 0 W to 3° at 1,000 W. This again indicates that the hot-wire preheating was sufficient to stabilize the single-bead condition, but not enough to fully suppress the complexity of the multi-bead pad.

Taken together, the IoU volatility and angle variability results suggest that the transition from erratic wire flutter to a more stable wire-melt-pool interaction is governed by the combined thermal condition of both features. Previous studies have described this transition as a shift toward improved thermal coupling, where sufficient melt-pool enthalpy and thermocapillary flow help to damp perturbations in the incoming wire and promote more repeatable incorporation into the molten region.[15,21] In this interpretation, a critical balance between wire momentum, wire preheating, and melt-pool flow is required to reduce flutter and effectively anchor the wire within the melt pool.[8,44] However, this mechanism should be interpreted as supported by the literature rather than directly measured in the present study, since the current analysis infers process stability from projected imaging geometry and therefore does not capture all components of the three-dimensional wire motion equally. Even with these limitations, the combined IoU, volatility, and angle variability results demonstrate that the wire dynamics provide a sensitive and practically useful indicator of process stability in LHW-DED.

The geometry dependence observed in this study also limits direct extrapolation of the stability thresholds to more complex deposition geometries. The IoU metrics themselves remain useful descriptors of wire motion because they quantify temporal changes in the segmented wire independently of a specific build geometry. However, the values associated with stable or unstable processes are expected to depend on the local thermal history, bead overlap strategy, surface topography, travel direction, and imaging geometry. In multi-layer or non-planar builds, heat accumulation and changes in surface orientation may further modify both features observed by the optical camera. Therefore, the identified laser and hot-wire power thresholds should be interpreted as geometry-dependent rather than universal LHW-DED stability values. The application of these metrics to multi-layer or complex geometries will require additional validation under the corresponding physical, geometrical, and imaging conditions.

3.3. Cross-sectional microscopy and Y–Z axis dimensional analysis

To complement the projected X–Y melt-pool measurements, post-process cross-sectional microscopy was used to quantify melt-pool geometry on the Y–Z plane. These measurements provide direct information about substrate penetration, fusion-zone geometry, and the final bead profile. Cross-sectional optical images were segmented using SAM2 to isolate the bead and fusion boundaries, from which bead width, bead height, dilution depth, bead area, dilution area, total cross-sectional area, and dilution ratio were extracted. These measurements provided a more direct representation of deposited and remelted material than the X–Y analysis alone.

Figure 12 shows the segmented cross-sectional melt-pool profiles for the laser power and hot-wire power variable conditions. Increasing laser power produced

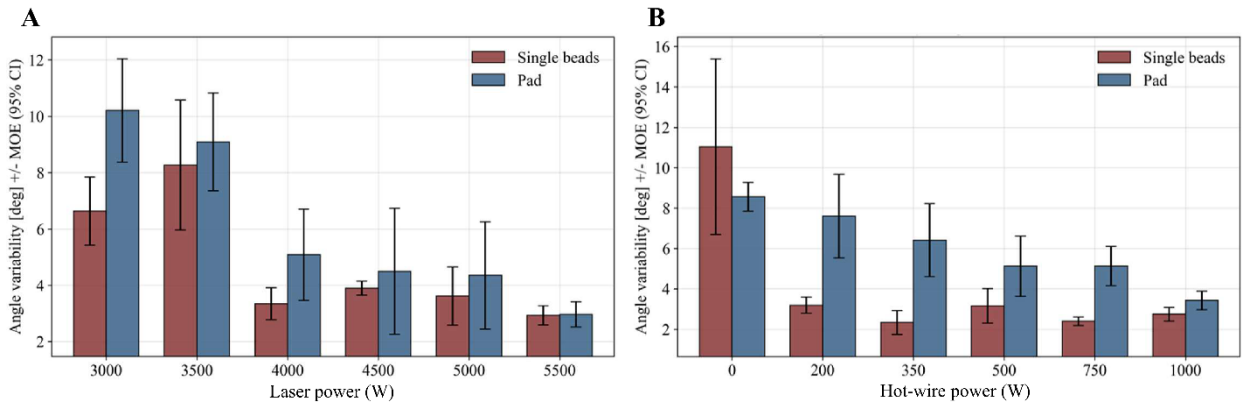


Figure 11. Wire angle variability values per printed geometry as a function of (A) laser power and (B) hot-wire power. Error bars represent 95% CIs. Higher angle variability indicates stronger fluctuations in the projected wire orientation, whereas lower values indicate more consistent wire alignment.
Abbreviations: CI: Confidence interval; MOE: Margin of error.

progressively deeper and larger fusion profiles, indicating stronger substrate interaction and greater penetration, whereas varying hot-wire power at constant laser power produced smaller geometric changes, with the most pronounced degradation occurring in the 0 W cold-wire condition. This contrast suggests that laser power and hot-wire power influenced the process through different physical pathways: laser power primarily governed fusion-zone growth and penetration, whereas hot-wire power mainly affected transfer stability and geometric repeatability.

3.3.1. Effect of laser power on the Y–Z melt-pool geometry

The dimensional analysis from the Y–Z cross-sectional measurements obtained under the laser-power conditions, with the hot wire fixed at 650 W, is summarized in the left columns of Figures 13 and 14. In contrast to the hot-wire sweep, laser power produced strong monotonic trends across the cross-sectional metrics. Dilution depth and dilution area increased approximately linearly with laser power, indicating deeper substrate melting and larger fusion volume as laser energy input increased. Bead width also increased with laser power, while bead height decreased slightly, consistent with enhanced wetting and lateral melt-pool spreading at higher energy input. As a result, bead area and total cross-sectional area increased with laser power, rising from approximately 8 mm^2 at 3,000 W to above 14 mm^2 at 5,500 W.

The dilution ratio also showed a strong dependence on laser power, increasing from approximately 0.14 at 3,000 W to approximately 0.44 at 5,500 W. This trend indicates a progressively greater substrate participation in the melt pool as laser power increased, consistent with the expected relationship between laser energy input, substrate melting, and dilution in laser DED processes.[21,45] These results confirm that laser power was the primary variable controlling the fusion zone growth and penetration in the Y–Z plane.

3.3.2. Effect of hot-wire power on the Y–Z melt-pool geometry

The quantitative trends for the hot-wire samples, performed at a constant laser power of 4,000 W, are summarized in the right columns of Figures 13 and 14. The cold wire condition produced the least stable geometry and the lowest values across several dimensional metrics. Increasing hot-wire power from 0 to 200 W produced the largest change in cross-sectional geometry, whereas further increases to 1,000 W resulted in comparatively consistent dimensional values. In particular, dilution depth and dilution area increased sharply from 0 to 200 W and then approached a plateau. Bead height and bead area showed a similar stabilization behavior, while bead width remained relatively constant across the hot-wire power range.

The total cross-sectional area also converged toward an approximately constant value once the preheating was introduced. These results indicate that hot-wire power primarily improved transfer consistency and bead repeatability rather than strongly increasing substrate penetration. This interpretation is consistent with the X–Y melt-pool area results, where hot-wire power produced

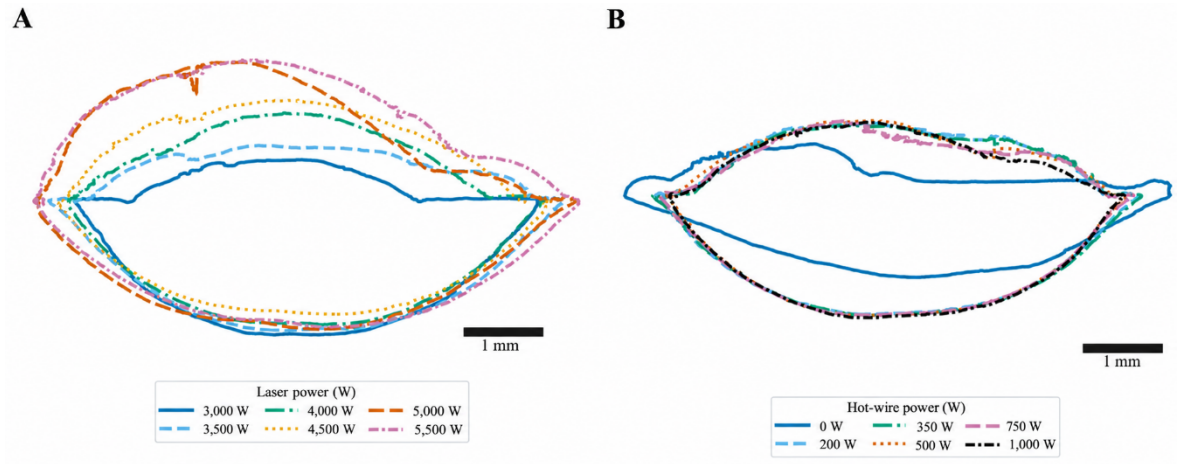


Figure 12. Y–Z plane melt-pool profiles extracted from cross-sectional optical microscopy. (A) Laser power varied from 3,000 to 5,500 W at a constant hot-wire power of 650 W. (B) Hot-wire power varied from 0 to 1,000 W at a constant laser power of 4,000 W. The contours represent the segmented bead and dilution boundaries for each process condition.

only a weak effect on the projected footprint once the preheating was introduced. The dilution-ratio behavior supports the same trend, where the cold wire condition showed lower and less consistent dilution, whereas hot-wire powers of 200 W and above produced a nearly constant dilution ratio. This response is consistent with the wire stability results in Section 3.2, where the 0 W condition produced low IoU, high volatility, and high angle variability, indicating unstable wire transfer. Similar instability mechanisms have been reported in cold wire processes, where insufficient wire enthalpy can promote intermittent transfer and poor wetting behavior.[45]

Thus, hot-wire power appears to function primarily as a wire-conditioning variable. Once sufficient preheating is introduced, the incoming wire interacts more consistently with the melt pool, reducing transfer instability and producing more repeatable Y–Z cross-sectional geometry. However, because laser power remained constant during this experiment, increasing hot-wire power did not produce the same increase in penetration or dilution observed in the laser power experiment. This confirms that, under the conditions studied, substrate penetration was governed primarily by laser power, while hot-wire power mainly stabilized material transfer and bead formation.[8]

3.4. Correlation between *in situ* monitoring metrics and *ex situ* geometries

The mean melt-pool area measured during the single-bead experiments was compared with the penetration depth and total cross-sectional area obtained from optical microscopy. In addition, the single-bead mean melt-pool area was compared with the corresponding mean frame-to-frame wire IoU for each laser-power condition. Pearson's correlation coefficient was used to quantify the linear associations, while statistical significance was assessed using an exact two-sided permutation test. Condition-level means were used to prevent the large number of temporally adjacent video frames from being treated as independent experimental observations.

The quantitative relationships are presented in Figures 15 and 16. As shown in Figure 15A, the mean penetration depth increased from approximately 0.46 mm at 3,000 W to 1.74 mm at 5,500 W as the mean *in situ* melt-pool area increased from approximately 18.30 to 23.37 mm^2. A statistically significant positive correlation was obtained between melt-pool area and penetration depth ($r = 0.954$, $p_{\text{exact}} = 0.0014$, $R^2 = 0.911$). A similar relationship was observed for the total cross-sectional area in Figure 15B. The total area increased from approximately 7.90 mm^2 at 3,000 W to 14.35 mm^2 at 5,500 W, resulting in $r = 0.962$, $p_{\text{exact}} = 0.0014$, and $R^2 = 0.926$. Figure 16 shows the relationship between melt-pool area and wire stability. The mean frame-to-frame IoU increased from approximately 35% at 3,000 W to approximately 90% at 4,000 W and remained between approximately 85% and 89% at higher laser powers. The melt-pool area and wire IoU were correlated ($r = 0.878$, $p_{\text{exact}} = 0.0069$, $R^2 = 0.771$).

These results indicate that the area identified through coaxial multi-Otsu segmentation is related to both the final cross-sectional geometry and the stability of the wire-transfer behavior. Although penetration depth cannot be directly observed from the coaxial camera view, the *in situ* melt-pool area strongly correlates with the mean penetration depth measured from the cross-sections, with the linear relationship explaining 91.1% of the variation among the laser power conditions. Similar relationships between real-time melt-pool geometry and cross-sectional characteristics, including penetration depth, have been reported for wire-based DED using image segmentation and statistical analysis.[33] The total cross-sectional area includes both the deposited material above the original substrate surface and the diluted region below it, providing an integrated measure of material deposition and substrate melting. Its strong relationship with the segmented melt-pool area suggests that the optical measurement can serve as an *in situ* process signature for estimating the final deposited geometry. This interpretation is aligned with previous coaxial monitoring studies that identified melt-pool area as a more reliable monitoring signal than average image intensity and demonstrated its suitability for maintaining stable deposition conditions.[22]

The relationship in Figure 16 indicates that melt-pool development and wire stability are coupled, particularly at the lower laser powers. At laser powers of 4,000 W and above, wire IoU entered a relatively stable range, while the melt-pool area continued to increase more gradually with laser power. Under low-power conditions, insufficient energy may limit wire-tip melting and anchoring, increasing wire flutter and producing less consistent material transfer into the melt pool. This motion may also perturb the melt-pool free surface and contribute to variability in the measured melt-pool area. Therefore, the observed correlation should be interpreted as evidence of an interaction between melt-pool development and wire behavior instead of a one-directional causal relationship.

An LOO sensitivity analysis was performed to evaluate whether the reported correlations were influenced by any individual laser-power condition (Table 2). For penetration depth, r remained between 0.941 and 0.987, with R^2 ranging from 0.886 to 0.974. Similarly, for total cross-sectional areas, r ranged from 0.952 to 0.986 and R^2 from 0.907 to 0.973. Removal of the 3,000 W condition did

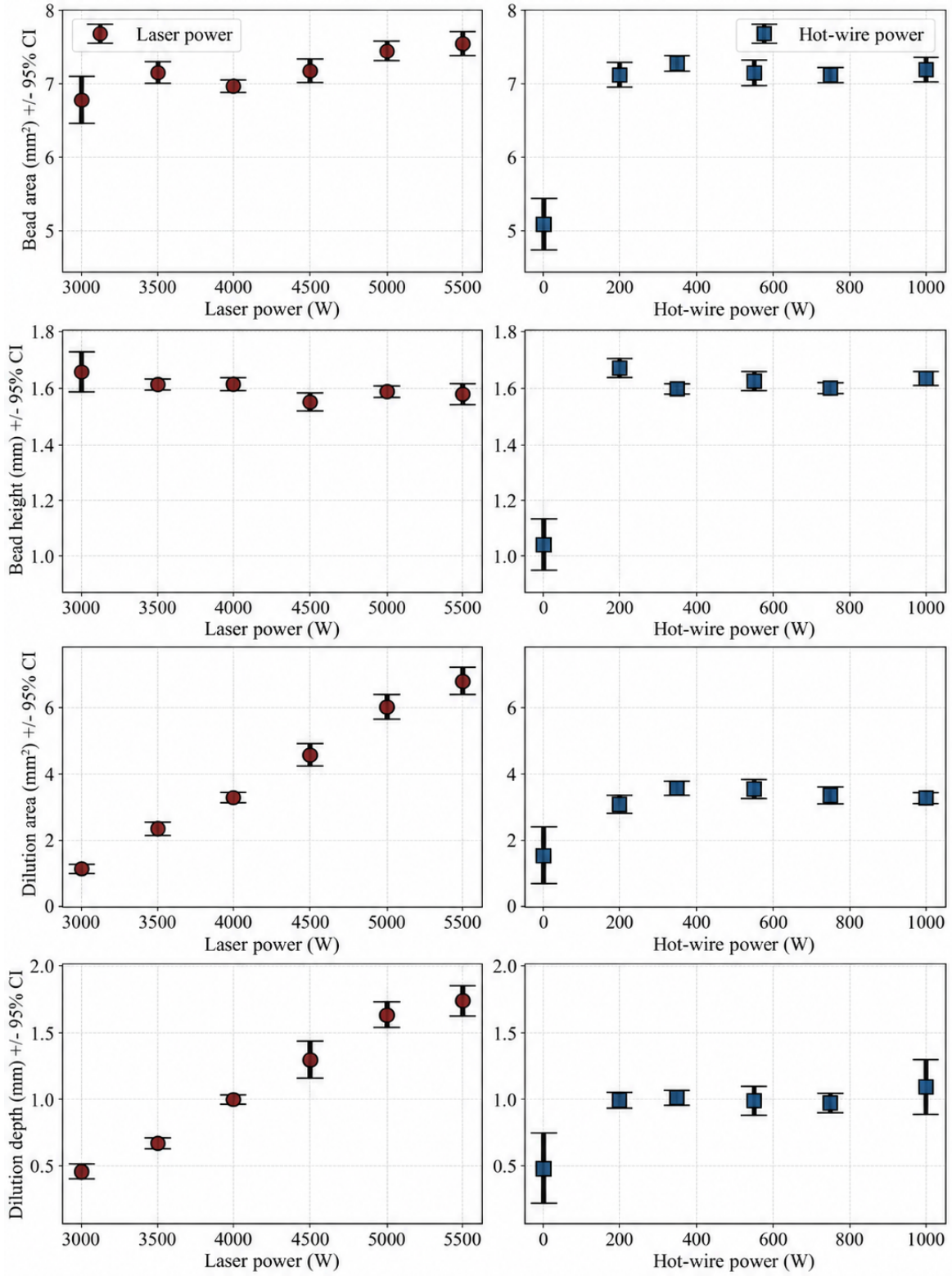


Figure 13. Evolution of bead area, bead height, dilution area, and dilution depth as a function of laser power and hot-wire power. The left column shows laser power variation at a constant hot-wire power of 650 W, while the right column shows hot-wire power variation at a constant laser power of 4,000 W. Abbreviation: CI: Confidence interval.

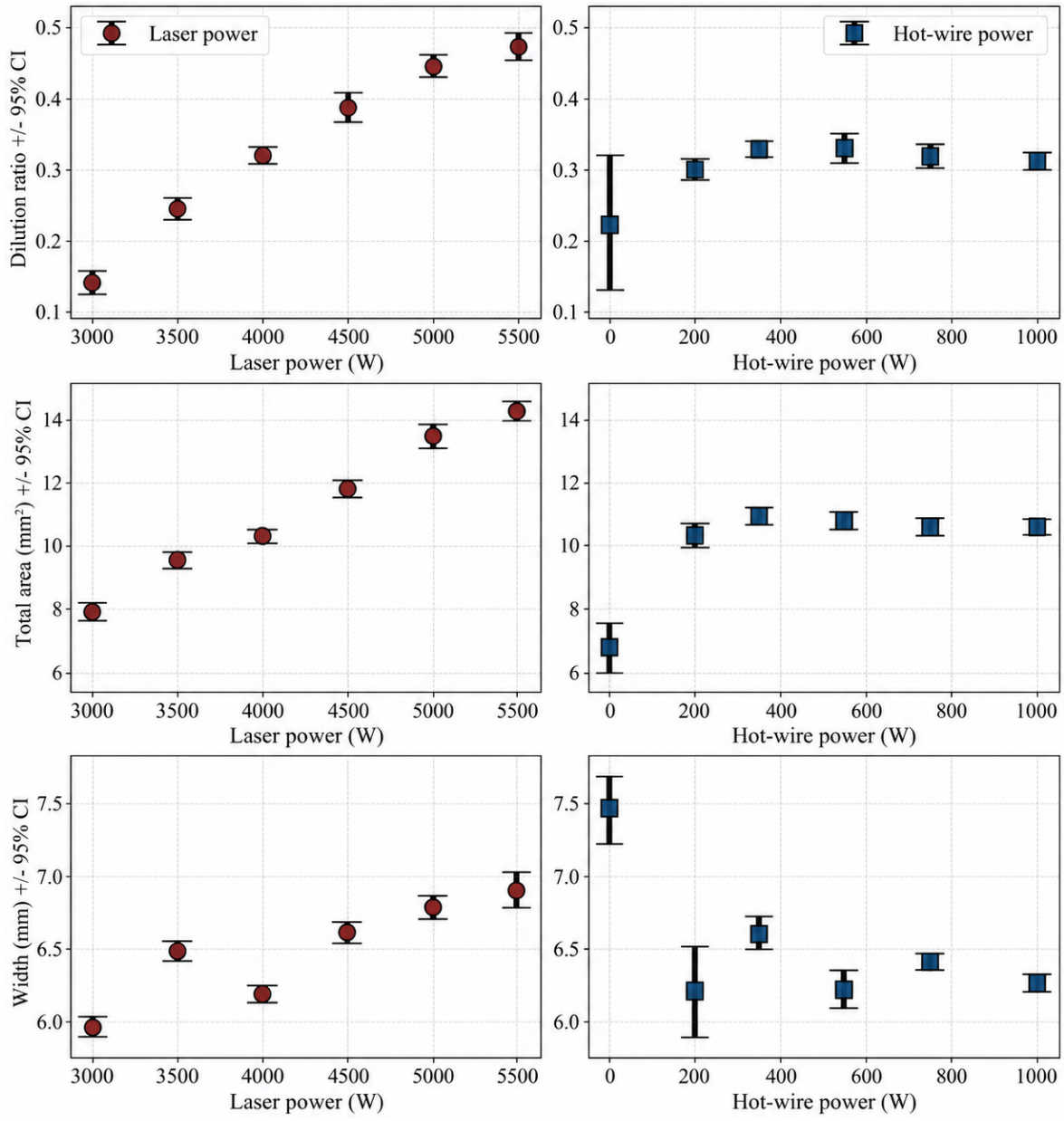


Figure 14. Evolution of dilution ratio, total cross-sectional area, and bead width as a function of laser power and hot-wire power. The left column shows laser-power variation at a constant hot-wire power of 650 W, while the right column shows hot-wire-power variation at a constant laser power of 4,000 W. Abbreviation: CI: Confidence interval.

not weaken these relationships and yielded r = 0.984 for penetration depth and r = 0.986 for total cross-sectional area. The relationship between melt-pool area and wire IoU showed greater sensitivity to individual condition removal. Across the LOO subsets, r ranged from 0.602 to 0.918 and R^2 from 0.362 to 0.842. The complete dataset yielded r = 0.823 and R^2 = 0.677, whereas excluding the 3,000 W condition produced the largest reduction in the correlation, with r = 0.602 and R^2 = 0.362. These sensitivity results suggest that the observed association is influenced by the transition from an unstable wire-transfer regime at lower laser power to a more stable regime at higher power. A similar pattern has been reported in wire-DED, where insufficient energy input resulted in increased wire oscillation and unstable transfer, whereas adequate thermal input promoted more continuous transfer into the melt

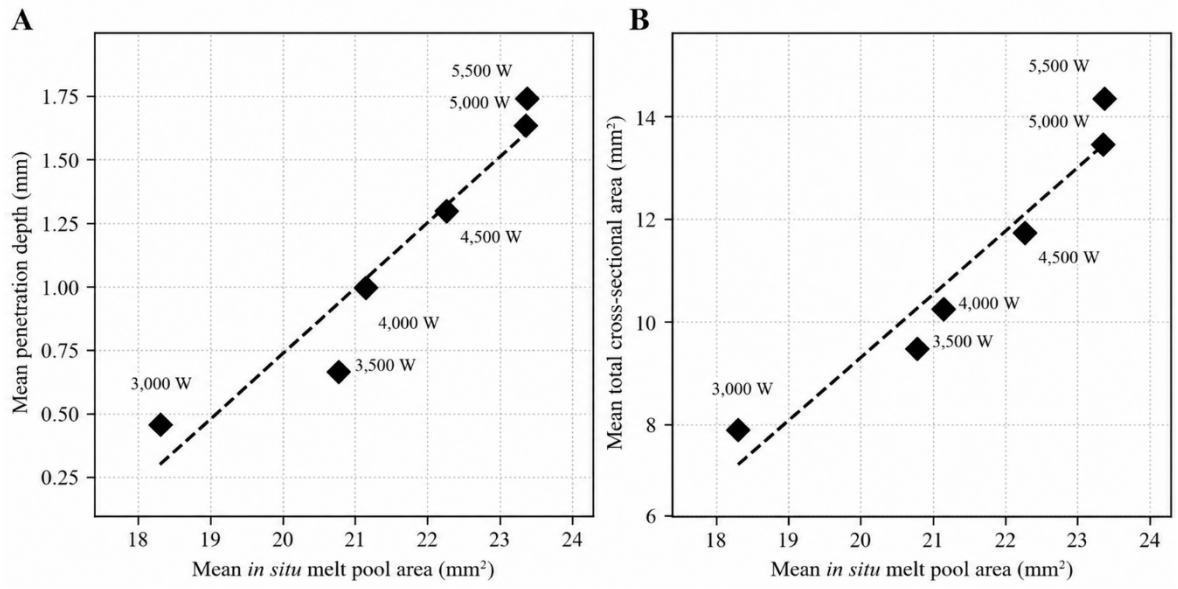


Figure 15. Correlation between the mean *in situ* melt-pool area and ex-situ cross-sectional geometry for the laser-power sweep on the single beads. (A) penetration depth and (B) total cross-sectional area. Markers represent condition means, and solid lines indicate linear regressions.

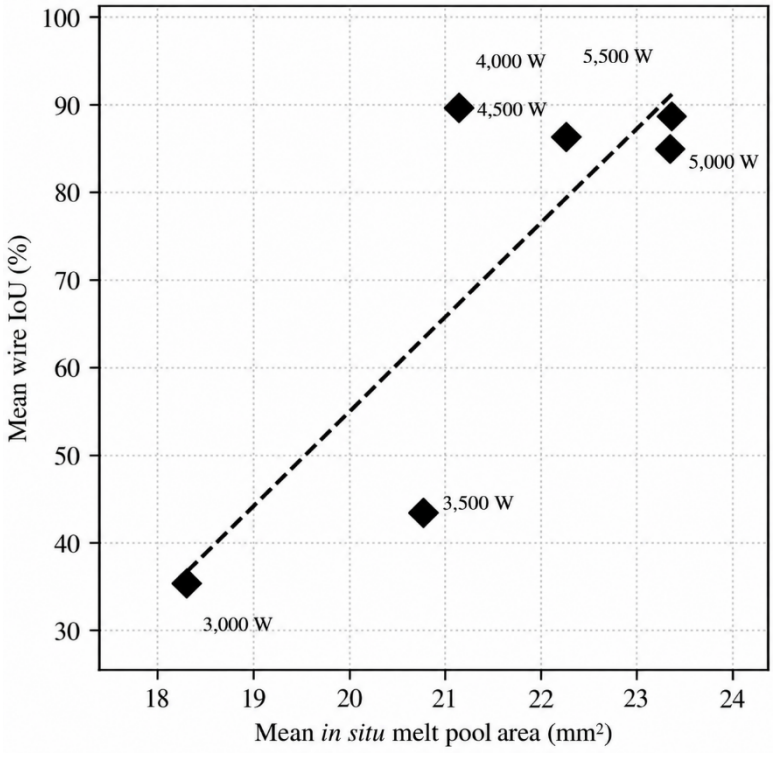


Figure 16. Correlation between the mean *in situ* melt-pool area and mean frame-to-frame wire Intersection over Union (IoU) for the single-bead laser-power sweep. Markers represent condition means, and the dashed line indicates the linear regression.

Table 2. Leave-one-condition-out sensitivity analysis for the condition-level correlations obtained from the single-bead laser-power sweep

Relationship	Full r	Full R^2	LOO r range	LOO R^2 range
Melt-pool area vs. penetration depth	0.954	0.911	0.941–0.987	0.886–0.974
Melt-pool area vs. total cross-sectional area	0.962	0.926	0.952–0.986	0.907–0.973
Melt-pool area vs. wire IoU	0.823	0.677	0.602–0.918	0.362–0.842

Note: The reported ranges represent the minimum and maximum values obtained after sequential removal of each laser-power condition.
Abbreviations: IoU: Intersection over Union; LOO: Leave-one-condition-out.

pool.[8,11] Future experiments should use finer energy-input increments around this transition to determine whether a reproducible stability zone can be identified.

4. Conclusion

This study established an image-based framework for evaluating process stability in LHW-DED by combining projected melt-pool geometry, wire dynamics analysis, and a post-process cross-sectional validation. The results show that laser power and hot-wire power influence the process through different mechanisms: Laser power was the primary driver of projected melt-pool growth and the resulting cross-sectional geometry, whereas hot-wire power acted mainly as a transfer-stabilization variable once a minimum preheating level was reached. The main conclusions are:

The projected melt-pool area increased with laser power for both the pad and single-bead geometries, confirming that the optical melt-pool footprint is a sensitive indicator of laser-power-driven changes. However, the response to hot-wire power was weaker and non-monotonic, showing that melt-pool area alone is not sufficient to evaluate process stability.

The 0 W hot-wire condition produced an enlarged but unstable melt-pool footprint, particularly during single bead deposition. This behavior was more consistent with cold-wire transfer and mechanical disturbance of the molten region than with improved thermal efficiency, demonstrating that a larger projected area does not necessarily indicate improved melting or greater process stability.

The SAM2-based segmentation analysis showed that the wire dynamics provide a complementary indicator of instability. Low stability conditions were associated with low IoU, high volatility, and elevated angle variability, while stable conditions showed higher frame-to-frame consistency and lower dynamic fluctuation.

The geometry-specific analysis showed that the stability transition depended on the deposition geometry. The single beads reached stable behavior at approximately 4,000 W laser power and at hot-wire powers ≥ 550 W, whereas the *in situ* indicators for the pad showed a comparable transition near 4,500 W. These transition values are specific to the analyzed geometries and process configuration and should not be interpreted as universal stability thresholds for LHW-DED.

The Y–Z cross-sectional analysis provided *ex situ* support for the *in situ* optical measurements. Across the laser-power conditions, the projected melt-pool area was strongly correlated with penetration depth ($r = 0.954$, $R^2 = 0.911$) and total cross-sectional area ($r = 0.962$, $R^2 = 0.926$). These relationships demonstrate that the coaxially measured melt-pool footprint contains information about both surface deposition and subsurface fusion. By contrast, hot-wire power primarily improved bead repeatability and stabilized the wire–melt-pool interaction, with limited additional influence on penetration after sufficient preheating was introduced.

The cross-sectional correlations remained stable under the LOO analysis, while the relationship between melt-pool area and wire IoU was more sensitive to the low-power stability transition.

This work shows that robust interpretation of process stability in LHW-DED requires joint analysis of melt-pool geometry and wire dynamics rather than evaluation of the projected melt-pool area alone. The observed correlations further demonstrate that the *in situ* optical measurements are related to both wire-transfer stability and the resulting cross-sectional geometry. Because these correlations were based on six condition-level means and the measured responses changed concurrently with laser power, they should be interpreted as associations rather than confirmed causal relationships. Future studies will extend the framework to multi-layer builds, where heat

accumulation is expected to play a larger role in melt-pool evolution, wire stability, and the definition of robust process windows.

Acknowledgments

The authors would like to highlight the support from the Murchison Chair at the University of Texas at El Paso. The authors would like to acknowledge the cooperation and support of the Mazak Corporation, Open Mind Technologies USA Inc., and Carl Zeiss Industrial Metrology LLC. The authors would also like to acknowledge Pablo Falcon, Katie Estrada, Whitney Watters, and Michael Mcallister. The authors also acknowledge Mazak Corporation for providing the LHW-DED system, Carl Zeiss Industrial Metrology LLC for providing the microscopy equipment, and OPEN MIND Technologies USA Inc. for providing the CAD/CAM software used in this study.

Funding

This material is based on research sponsored by Air Force Research Laboratory under Agreement Number FA8650-20-2-5700. The U.S. Government is authorized to reproduce and distribute reprints for Governmental purposes notwithstanding any copyright notation thereon. This research was supported in part by an appointment to the Oak Ridge National Laboratory GRO Program, sponsored by the U.S. Department of Energy and administered by the Oak Ridge Institute for Science and Education. This work was supported by the US Department of Energy, Office of Energy Efficiency and Renewable Energy, Advanced Materials and Manufacturing Technologies Office under contract number DE-AC05-00OR22725.

Conflict of interest

The views and conclusions contained in this document are those of the authors and should not be interpreted as necessarily representing the official policies or endorsements, either expressed or implied, of the Air Force Research Laboratory or the U.S. Government.

Author contributions

Conceptualization: Mario Rodriguez-Parra, Mithulan Paramanathan, Miguel Hoffmann
Formal analysis: Mario Rodriguez-Parra
Funding acquisition: Thomas Feldhausen, Eric MacDonald
Investigation: Mario Rodriguez-Parra, Miguel Hoffmann
Methodology: Mario Rodriguez-Parra, Mithulan Paramanathan
Supervision: Thomas Feldhausen, Eric MacDonald
Writing–original draft: Mario Rodriguez-Parra
Writing–review & editing: Mario Rodriguez-Parra, Miguel Hoffmann, Eric MacDonald, Thomas Feldhausen

Ethics approval and consent to participate

Not applicable.

Consent for publication

Not applicable.

Availability of data

The data presented in this study are available from the corresponding author upon reasonable request.

Further disclosure

The results presented in Sections 3.1 and 3.2 of this paper were previously presented at the 36th Annual International Solid Freeform Fabrication Symposium (SFF 2025), held August 10–13, 2025, in Austin, Texas, USA.

References

1. Hoffmann M, Heinrich L, Paramanathan M, Fillingim KB, Elwany A, Feldhausen T. Hybrid additive manufacturing of AISI 316L via asynchronous powder and hot-wire laser directed energy deposition. *J Manuf Processes.* 2024;127:446-456.

   doi: 10.1016/j.jmapro.2024.07.144

2. F42 Committee. Terminology for Additive Manufacturing—General Principles—Terminology.

   doi: 10.1520/ISOASTM52900-15

3. Pinkerton AJ. Laser direct metal deposition: theory and applications in manufacturing and maintenance. In: *Advances in Laser Materials Processing*. Elsevier; 2010:461-491.

   doi: 10.1533/9781845699819.6.461

4. Stawovy MT. Comparison of LCAC and PM Mo deposited using Sciaky EBAM™. *Int J Refract Met Hard Mater.* 2018;73:162-167.

   doi: 10.1016/j.ijrmhm.2018.02.009

5. Duda T, Raghavan LV. 3D Metal Printing Technology. *IFAC-PapersOnLine*. 2016;49(29):103-110.

   doi: 10.1016/j.ifacol.2016.11.111

6. Wu B, Pan Z, Ding D, *et al.* A review of the wire arc additive manufacturing of metals: properties, defects and quality improvement. *J Manuf Processes*. 2018;35:127-139.

   doi: 10.1016/j.jmapro.2018.08.001

7. Abranovic B, Chang-Davidson E, Beuth JL. Process mapping for laser hot wire additive manufacturing of Ti6Al4V. *Rapid Prototyp J.* 2025;31(6):1156-1174.

   doi: 10.1108/RPJ-05-2024-0216

8. Kisielewicz A, Thalavai Pandian K, Sthen D, *et al.* Hot-Wire Laser-Directed Energy Deposition: Process Characteristics

and Benefits of Resistive Pre-Heating of the Feedstock Wire. *Metals*. 2021;11(4):634.

doi: 10.3390/met11040634

9. Ghanadi N, Pasebani S. A Review on Wire-Laser Directed Energy Deposition: Parameter Control, Process Stability, and Future Research Paths. *JMMP*. 2024;8(2):84.

doi: 10.3390/jmmp8020084

10. DebRoy T, Wei HL, Zuback JS, *et al.* Additive manufacturing of metallic components – Process, structure and properties. *Prog Mater Sci.* 2018;92:112-224.

doi: 10.1016/j.pmatsci.2017.10.001

11. McLain B, Mathenia R, Sparks T, Liou F. Machine Vision to Provide Quantitative Analysis of Meltpool Stability for a Coaxial Wire Directed Energy Deposition Process. *Materials*. 2024;17(21):5311.

doi: 10.3390/ma17215311

12. Akbari M, Ding Y, Kovacevic R. Process Development for a Robotized Laser Wire Additive Manufacturing. In: *Volume 2: Additive Manufacturing; Materials*. American Society of Mechanical Engineers; 2017:V002T01A015.

doi: 10.1115/MSEC2017-2951

13. Heralić A, Christiansson AK, Lennartson B. Height control of laser metal-wire deposition based on iterative learning control and 3D scanning. *Opt Lasers Eng.* 2012;50(9):1230-1241.

doi: 10.1016/j.optlaseng.2012.03.016

14. Motta M, Demir AG, Previtali B. High-speed imaging and process characterization of coaxial laser metal wire deposition. *Addit Manuf.* 2018;22:497-507.

doi: 10.1016/j.addma.2018.05.043

15. Liu S, Liu W, Harooni M, Ma J, Kovacevic R. Real-time monitoring of laser hot-wire cladding of Inconel 625. *Opt Laser Technol.* 2014;62:124-134.

doi: 10.1016/j.optlastec.2014.03.007

16. Hagqvist P, Heralić A, Christiansson AK, Lennartson B. Resistance measurements for control of laser metal wire deposition. *Opt Lasers Eng.* 2014;54:62-67.

doi: 10.1016/j.optlaseng.2013.10.010

17. Ding D, Pan Z, Cuiuri D, Li H. Wire-feed additive manufacturing of metal components: technologies, developments and future interests. *Int J Adv Manuf Technol*. 2015;81(1-4):465-481.

doi: 10.1007/s00170-015-7077-3

18. Bernauer C, Merk T, Zapata A, Zaeh MF. Laser Metal Deposition with Coaxial Wire Feeding for the Automated and Reliable Build-Up of Solid Metal Parts. *KEM*. 2022;926:65-79.

doi: 10.4028/p-ob7dg7

19. Wei S, Wang G, Shin YC, Rong Y. Comprehensive modeling of transport phenomena in laser hot-wire deposition process. *Int J Heat Mass Transf.* 2018;125:1356-1368.

doi: 10.1016/j.ijheatmasstransfer.2018.04.164

20. Feng S, Wainwright J, Wang C, *et al.* Video Segmentation of Wire + Arc Additive Manufacturing (WAAM) Using Visual Large Model. *Sensors*. 2025;25(14):4346.

doi: 10.3390/s25144346

21. Sun Z, Guo W, Li L. In-process measurement of melt pool cross-sectional geometry and grain orientation in a laser directed energy deposition additive manufacturing process. *Opt Laser Technol.* 2020;129:106280.

doi: 10.1016/j.optlastec.2020.106280

22. Da Silva A, Frostevarg J, Kaplan AFH. Melt pool monitoring and process optimisation of directed energy deposition via coaxial thermal imaging. *J Manuf Processes* 2023;107:126-133.

doi: 10.1016/j.jmapro.2023.10.021

23. Gibson BT, Bandari YK, Richardson BS, *et al.* Melt pool monitoring for control and data analytics in large-scale metal additive manufacturing. In: Solid Freeform Fabrication 2019: Proceedings of the 30th Annual International Solid Freeform Fabrication Symposium – An Additive Manufacturing Conference. Accessed May 1, 2026. https://utw10945.utweb.utexas.edu/sites/default/files/2019/122%20Melt%20Pool%20Monitoring%20for%20Control%20and%20Data%20Analytic.pdf

24. Kledwig C, Perfahl H, Reisacher M, Brückner F, Bliedtner J, Leyens C. Analysis of Melt Pool Characteristics and Process Parameters Using a Coaxial Monitoring System during Directed Energy Deposition in Additive Manufacturing. *Materials*. 2019;12(2):308.

doi: 10.3390/ma12020308

25. Pandiyan V, Cui D, Richter RA, Parrilli A, Leparoux M. Real-time monitoring and quality assurance for laser-based directed energy deposition: integrating co-axial imaging and self-supervised deep learning framework. *J Intell Manuf*. 2025;36(2):909-933.

doi: 10.1007/s10845-023-02279-x

26. Li J, Zhou Q, Huang X, Li M, Cao L. In situ quality inspection with layer-wise visual images based on deep transfer learning during selective laser melting. *J Intell Manuf*. 2023;34(2):853-867.

doi: 10.1007/s10845-021-01829-5

27. Hu D, Kovacevic R. Sensing, modeling and control for laser-based additive manufacturing. *Int J Mach Tools Manuf.* 2003;43(1):51-60.

doi: 10.1016/S0890-6955(02)00163-3

28. Zhang Y, Shen S, Li H, Hu Y. Review of in situ and real-time

monitoring of metal additive manufacturing based on image processing. *Int J Adv Manuf Technol*. 2022;123(1-2):1-20.

doi: 10.1007/s00170-022-10178-3

29. Shah A, Weissbach R, Griggs DA, Hart AJ, Ertekin E, Tawfick S. Automated segmentation and analysis of microscopy images of laser powder bed fusion melt tracks. *J Manuf Processes*. 2025;154:61-70.

doi: 10.1016/j.jmapro.2025.09.043

30. Zhang K, Zhao T, Chen M, Zhang J, An Q. Improved U-net network with temporal adaptive Module for precise melt pool detection in LDED additive manufacturing. *J Manuf Processes*. 2025;153:650-664.

doi: 10.1016/j.jmapro.2025.09.014

31. De M, Dutta S, Mukherjee M. Enhanced *in situ* monitoring of metal deposition behaviour for pulsed wire arc directed energy deposition using integrated noncoaxial imaging and supervised deep learning framework. *Sci Rep*. 2025;15(1):42003.

doi: 10.1038/s41598-025-26001-4

32. He K, Gkioxari G, Dollár P, Girshick R. Mask R-CNN. *arXiv*. Preprint posted online 2017.

doi: 10.48550/arXiv.1703.06870

33. Asadi R, Queguineur A, Wiikinkoski O, *et al.* Process monitoring by deep neural networks in directed energy deposition: CNN-based detection, segmentation, and statistical analysis of melt pools. *Robot Comput Integr Manuf*. 2024;87:102710.

doi: 10.1016/j.rcim.2023.102710

34. Era IZ, Zhou F, Raihan AS, *et al. In situ* melt pool characterization via thermal imaging for defect detection in Directed Energy Deposition using Vision Transformers. *J Manuf Processes*. 2025;145:11-21.

doi: 10.1016/j.jmapro.2025.03.123

35. Kirillov A, Mintun E, Ravi N, *et al.* Segment Anything. *arXiv*. Preprint posted online 2023.

doi: 10.48550/arXiv.2304.02643

36. Ravi N, Gabeur V, Hu YT, *et al.* SAM 2: Segment Anything in Images and Videos. *arXiv*. Preprint posted online 2024.

doi: 10.48550/arXiv.2408.00714

37. Carion N, Gustafson L, Hu YT, *et al.* SAM 3: Segment Anything with Concepts. *arXiv*. Preprint posted online 2025.

doi: 10.48550/arXiv.2511.16719

38. Liao PS, Chen TS, Chung PC. A fast algorithm for multilevel thresholding. *J Inf Sci Eng*. 2001;17(5):713-717.

doi: 10.6688/JISE.2001.17.5.1

39. Chen J, Li H, Shen S, *et al.* Universal light SAM algorithm for in situ melting pool monitoring of L-DED/L-PBF/PAM processes. *J Comput Des Eng*. 2025;12(7):35-48.

doi: 10.1093/jcde/qwaf057

40. Bernauer C, Leitner P, Zapata A, *et al.* Segmentation-based closed-loop layer height control for enhancing stability and dimensional accuracy in wire-based laser metal deposition. *Robot Comput-Integr Manuf*. 2024;86:102683.

doi: 10.1016/j.rcim.2023.102683

41. Asadi R, Queguineur A, Ituarte IF. CNN-Based Wire Monitoring in LW-DED: Correlation with Surface Metrology. *IOP Conf Ser Mater Sci Eng*. 2025;1332(1):012039.

doi: 10.1088/1757-899X/1332/1/012039

42. Zhao Y, Sun J, Zhang G, Sun F, Li H. Enhancing SAM2 for Industrial Defect Detection via Dual-Adapter Fine-Tuning. *IEEE Trans Instrum Meas*. 2026;75:5009413.

doi: 10.1109/tim.2026.3693442

43. Putz F, Beirami S, Schmidt MA, *et al.* The Segment Anything foundation model achieves favorable brain tumor auto-segmentation accuracy in MRI to support radiotherapy treatment planning. *Strahlenther Onkol*. 2025;201(3):255-265.

doi: 10.1007/s00066-024-02313-8

44. Bambach M, Sizova I, Kies F, Haase C. Directed energy deposition of Inconel 718 powder, cold and hot wire using a six-beam direct diode laser set-up. *Addit Manuf*. 2021;47:102269.

doi: 10.1016/j.addma.2021.102269

45. Zhang K, Zhang XM, Liu WJ. Influences of Processing Parameters on Dilution Ratio of Laser Cladding Layer during Laser Metal Deposition Shaping. *Adv Mater Res*. 2012;549:785-789.

doi: 10.4028/www.scientific.net/AMR.549.785